Electronic Supplementary Information (ESI)

Hierarchical nanotwins in single-crystal-like Nickel with high strength and corrosion resistance produced *via* a hybrid technique

Qiang Li[a], Sichuang Xue[a], Patrick Price[b], Xing Sun[a], Jie Ding[a], Zhongxia Shang[a], Zhe Fan[c], Han Wang[a], Yifan Zhang[a], Youxing Chen[d], Haiyan Wang[a,e], Khalid Hattar[b] and Xinghang Zhang[a,]*

[a] School of Materials Engineering, Purdue University, West Lafayette, IN 47907, United States

[b] Sandia National Laboratories, Albuquerque, NM 87185, United States

[c] Materials Science and Technology Division, Oak Ridge National Laboratory, Oak Ridge, TN 37831, United States

[d] Department of Mechanical Engineering and Engineering Science, University of North Carolina at Charlotte, Charlotte, NC 28223, United States

[e] School of Electrical and Computer Engineering, Purdue University, West Lafayette, IN 47907, United States

[*] Corresponding author: xzhang98@purdue.edu

Experimental

Firstly, a 1 μm-thick (111)-textured Cu layer was sputtered on a silicon (110) wafer (1 inch × 2 inch), pretreated by ~ 48 % hydrofluoric acid, in ATC flagship sputtering system (AJA international, Inc.) at a base pressure of 1-2 × 10^{-8} Torr using Cu (99.99%) target. The epitaxial Cu acts as both underlying conducting medium and growth template for Ni prepared by either sputtering or electrodeposition technique. The purpose of precisely controlled projected dimensions of Si wafer is to control the effective current density during electrodepositions. In monolithic sputtering technique, Ni (99.99%) was subsequently sputtered onto Cu (111) templates at room temperature. In hybrid sputtering and electrodeposition method, the Cu (111) templates on Si (110) or polycrystalline Cu on 100 nm-thick SiO_2-coated Si(100) wafers were adopted as cathode electrodes for electrodepositions conducted on a Dynatronix DPR40-15-30XR, a galvanostat pulse reserving current supply. A typical electrodeposition was done in a water bath held isothermally at ~ 45 ˚C at an effective current density, $\bar{J}_{average}$, of 60-80 mA/cm^2 when pulse-on duration, t_{on}, and pulse-off duration (0 mA/cm^2), t_{off}, were 2 ms and 2 ms, respectively. The cathode and high-purity Ni plate as anode were immersed in electrodeposition bath for 1 inch^2 and kept at a 4 cm separation distance. Ni anode continuously replenished the consumed ions in bath. The electrodeposition electrolyte was composed of 0.85 M nickel (II) chloride hexahydrate ($NiCl_2 \cdot 6H_2O$), 0.065 M nickel (II) sulfamate tetrahydrate ($Ni(SO_3NH_2 \cdot 4H_2O$) and 0.4 M boric acid (H_3BO_3) (Chemicals were purchased from Alfa Aesar). 0.005 M sodium saccharin was selectively added to electrolyte to control microstructure. The hybrid technique and monolithic sputtering technique are laid out in Figure S1.

In situ SEM compression experiments

In situ uniaxial compression experiments were carried out using a Hysitron PI 88 PicoIndenter with a 5 μm diamond flat punch indenter inside an FEI quanta 3D FEG scanning electron microscope (SEM). A piezoelectric actuator on the capacitive transducer captured the force-displacement responses. A strain rate of 5.0×10^{-3}/s was constantly used in a displacement-control mode. To circumvent the issue of indenter-pillar misalignment, an "impact crater" method was introduced. Summarily, the dihedral angle of sample surface and circular depression surface created by flat punch indenter on sample was measured. Alignment was correspondingly adjusted through rotation and tilting of sample stage. Partial unloading segments were incorporated to verify alignment reliability. 50 μN force was applied upon pillars for 40 s to correct the drift, estimated at 0.1-0.4 nm/s. The displacement and force noise levels were detected to be ± 0.35 nm/s and ± 5 μN on average, respectively. Micropillars with a diameter-to-height aspect ratio of 1:3-1:2 were made using a dual-beam FEI Quanta 3D FEG SEM. A series of concentric annular focused ion beam (FIB) milling and polishing with progressively de-escalated currents from 15 nA to 10 pA were used. A bi-directional FIB polishing was required to flatten the heads of micropillars of specimens with serious surface roughness. To avoid the influence from the underlying Cu, the micropillars were fabricated on thick films and the base material is mostly Ni. For each sample, at least 5 micropillars were compressed for repeatability check.

Corrosion measurement

The potentiodynamic polarization measurements were carried out in a three-electrode cell. A saturated calomel electrode (SCE) *via* E (*vs*. SCE) = E (*vs*. SHE) - 0.241 V and a graphite rod were used as reference and counter electrodes, respectively. Various nickel films were used as

working electrodes. The working electrodes were prepared by fastening Ni specimen to Cu plate with conductive Ag paste and sealing by PortHole (an electroplating mask; 3″ × 3″; 11.3 mm diameter hole = 1 cm^2). Prior to polarization tests, the working electrodes were rinsed by acetone and purified water and then stabilized in corrosion solute for 20 min to reach a linear relationship around corrosion potential. Due to the substantial surface roughness of cg Ni prepared by hybrid technique, bulk polycrystalline cg Ni foil with an average grain size of ~ 60 μm was used to represent corrosion behaviors of cg Ni. Measurements were performed in an artificial seawater, namely 3.5 *wt.*% of NaCl solutions with a PH value of 7.8 ± 0.2 at room temperature, using a Gamry 1000 Potentiostat/Galvanostat workstation. Potentiodynamic polarization curves were acquired at a scan rate of 1.0 mV/s and the corrosion potential (E_{corr}), corrosion current density (i_{corr}) and anodic/cathodic Tafel slops (B_a and B_c) were determined by Tafel extrapolation method. The polarization resistance (R_p) were determined from Stern-Geary equation [1]:

$$R_p = \frac{B_a B_c}{2.303 i_{corr}(B_a + B_c)} \quad (1)$$

Corrosion rate (V_{corr}) were derived by polarization curves using Gamry Echem Analyst software.

Characterizations

Automated crystal orientation mappings (ACOM) on nanotwinned Ni were acquired on the Nanomegas ASTAR mapping apparatus equipped on a JEOL 2100 transmission electron microscope (TEM) as well as a Talos 200X TEM. Orientation maps were collected in TEM diffraction mode with a 10 μm condenser aperture, 4 nm step size, 0.5° procession angle, alpha 3,

and spot size 5. Collected serial diffraction patterns were matched to the Ni Fm-3m structure to determine orientation. X-ray diffraction (XRD) patterns were acquired on a Panalytical Empyrean X'pert PRO MRD diffractometer with a Cu Kα1 source. X-ray pole figures were collected using the tube-in-line focus and capillary X-ray lens with a spot opening of 1×1 mm^2 on the primary optics and parallel plate collimator on the detector side. TEM imaging was performed on Talos 200X microscope at 200 kV, equipped with Fischione ultra-high resolution high angle annular dark field (HADDF) detectors and supper X electron-dispersive x-ray spectroscopy (EDS). Plan-view TEM samples were prepared using grinding, followed by dimpling and low-energy ion milling, and cross-section TEM samples were lifted out and mounted to Molybdenum grids using Omniprobe AutoProbe^{TM} lift-out tool and eventually thinned to ~ 100 nm at 2 kV as a final ion acceleration voltage.

Interpretation towards true stress-strain curves

The interpretation of true tress-strain behaviors by micropillar compression tests is intricate because of the fact that the indenter-pillar contact area variation upon deformation is material-sensitive and it is instantaneous and different depending on the response of intrinsic microstructure to the stress in various Ni samples. This inevitably brings challenge to interpret hardening and softening inside deformed materials. Therefore, a numerical model for *in situ* SEM compressions is developed to elucidate the deformation behaviors of the various Ni specimens in this study, whose deformation geometry is different from the homogeneous deformation model where the height and diameter of cylindrical micropillars are considered uniformly evolving.

Firstly, the influence of elastic compliance of base material and the diamond flat punch indenter on the measured displacement is taken into account. The valid displacement is corrected according to Sneddon method as [2]:

$$u = u_{mea} - \frac{1 - v_{dia}^2}{E_{dia}}\left(\frac{F}{d_0}\right) - \frac{1 - v_{base}^2}{E_{base}}\left(\frac{F}{d_r}\right) \quad (2)$$

where u_{mea}, F are the measured displacement and force, respectively. d_0, d_r stand for diameter measured at the top and the root of the micropillars, respectively. E_{dia} and ν_{dia} represent the elastic modulus and Poisson ratio of the diamond indenter, respectively; meanwhile the E_{base} and ν_{base} represent the elastic modulus and Poisson ratio of the base material.

After influence on displacement from indenter-pillar friction and pillar-base constraint is corrected, the displacement, u, consists of elastic, u_e, and plastic displacement, u_p is:

$$u = u_e + u_p = \frac{P}{K_{pu}} + u_p \quad (3)$$

where K_{pu} is the slope of the partial unloading intentionally added into elastic regimes as load function was set. The spontaneous diameter, d_s, of micropillars for homogeneous deformation model is (at the assumption of conserved volume, *i.e.* $A_0H_0 = A_sH_s$, where A_0, H_0, A_s and H_s is initial contact area, initial micropillar height, spontaneous contact area and spontaneous micropillar height, respectively) [3]:

$$d_s = d_0\sqrt{\frac{H_0}{H_0 - (u - P/K_{pu})}} \quad (4)$$

Attributing the spontaneous diameter measurement to the ability of *in situ* SEM imaging that captures real-time deformation geometry, we could establish the relation between d_s and u to evaluate spontaneous true stress by measuring spontaneous diameter at the indenter-pillar contact. The spontaneous true stress can be simply expressed as $\sigma_T = 4P/\pi d_s^{\,2}$ at a certain value of (u – P/K_{pl}) (Figure S11). And the true strain can be expressed as $\varepsilon_T = -\ln(1 - u/H_0)$. The hardening rate based on spontaneous true stress-strain curves was calculated by taking the slope of the flow stress increment over strain increment at 5 – 12 %.

Confined layer slip (CLS) model

Anisotropic deformation behaviors have been previously investigated on textured nt metals, mostly nt Cu with columnar grains and preferentially oriented twin structures. It was found that dislocation movement with respect to twin boundaries, yield strength and strain working strongly depend on loading directions. Particularly, as compressive stress direction is perpendicular to CTBs, activated slip plane and slip direction are inclined to CTBs and the strengthening accurately complies with Hall-Petch relation and deformation carriers are dislocation pile-up and cutting through CTBs. And dislocation glide along CTBs, expressed as confined layer slip (CLS) mode, happens while loading direction is parallel to CTBs. Meanwhile, it should to be realized that Hall-Petch relation becomes invalid when microstructural feature size drops to a few nanometers or tens of nanometers as elasticity-based calculation states that it requires a minimum of 6 single-ended dislocations to fulfill $\sigma \propto d^{-1/2}$. Within the nanometer length scale, single dislocation glides between phase interfaces or TBs similarly to Orowan-type

dislocation bowing, defined as confined layer slip (CLS) mode. The CLS strengthening is expressed as follows:

$$\sigma_{CLS} = M\frac{\mu b \sin\theta}{8\pi t}\left(\frac{4-\nu}{1-\nu}\right)\left[ln\frac{\alpha t}{b\sin\theta}\right] \quad (2)$$

where t and α denote the twin spacing and dislocation core cutoff parameter, respectively, and θ is the angle of 70.53 ° between the inclined and horizontal glide planes, *i.e.* (111) and $(\bar{1}11)$ planes. Given that shear modulus $\mu = 76$ GPa, Burgers vector b = 0.25 nm, Poisson's ratio ν = 0.31 and a Taylor factor of 3 is applied, the CLS stress, σ_{CLS}, is estimated as a function of twin spacing, t. It is worth mentioning the core cutoff parameter, α, is variable and depend on the spreading distance of dislocation core along interface/boundary. The incoherent nanolaminate interfaces have lower resistance to interfacial sliding, and thus the dislocation cores spread along interfaces to minimize core energy. The dislocation cut-off distance is b/α. For instance, Cu/Nb multilayers use a cut-off distance of b/0.2 and Ti/Ni multilayers of b/0.16. It means that a compact core constrained within a Burgers vector will have α equal to 1. That is to say that the α value for a monolithic Ni with CTBs can be safely situated in the range of 0.2-1. In Figure S8, CLS strengthening curves with α = 0.2 and α = 1 are incorporated into the Hall-Petch plot to tentatively comprehend the extra hardening in e-nt Ni.

Strain-related perspective on twin formation in e-nt Ni

Besides twin formation mechanism stated in main text, the strain developed in growth process may have influence on twin formation in e-nt Ni. For example, the inclined twin formation in cg Ni is considered energetically unfavorable. To be specific, for a 5 nm-thick inclined twin that propagates through a 2 μm-thick film in Figure S5f, provided that the CTB energy, γ_{Ni}^{CTB}, in Ni is 63 mJ/m^2 and the energy of ∑5{310} GBs is taken as the ITB energy, γ_{Ni}^{ITB},

i.e. 1469 mJ/m^2, the energy carried by the CTBs bounding the twin lamella is $4\times10^{-6}\gamma_{Ni}^{CTB}/\sin70.53^{\circ}$, equal to ~ 2.67×10^{-4} mJ/m, whereas the energy an ITB bears is $5\times10^{-9}\gamma_{Ni}^{ITB}/\sin70.53^{\circ}$, equal to ~ 7.35×10^{-6} mJ/m if a growth twin terminates inside grain interior [4]. Hence, the energetically unfavorable twin propagation might alleviate the strain energy. Also, the nc Ni has a preferential (100) texture with the lowest strain energy. Moreover, it is found that the ITB segment in e-nt Ni often have dissociative character, *i.e.* 9R phase, which is a high energy defect but carries no extra strain energy due to the zero net Burgers vectors of the three repeatable Shockley partials [5, 6]. Those hints suggest that microstructural development in Ni specimens might be influenced by the strain energy. Independent studies might need to be dedicated to reveal more insights into the mechanism.

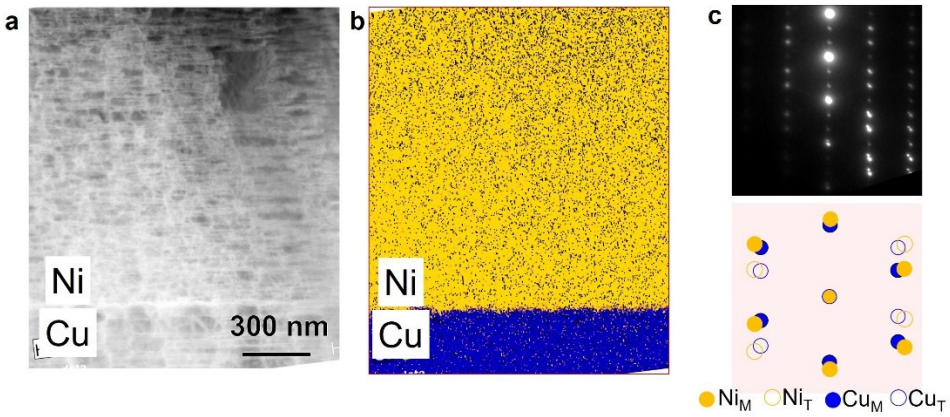

Figure S1. (a) HAADF-STEM image and (b) energy dispersive X-ray spectroscopy (EDS) compositional mapping of e-nt Ni. 1 µm-thick (111)-textured Cu was sputtered on 500 µm-thick Si(110) substrates and used as cathode electrodes. Ni grew on Cu (111) using electrodeposition in aqueous electrolyte with organic additive. (c) SAD pattern taken at the Cu and Ni interface indicating nt Ni (111) using hybrid technique could heteroepitaxially grow on nt Cu (111). The measured chemical composition (at.%) of e-nt Ni prepared by electrodeposition with organic additive on Cu (111) is 98.02 ± 0.1 Ni, 1.1 ± 0.7 C, 0.33 ± 0.1 N, 0.42 ± 0.2 O and 0.14 ± 0.1 S. Note that the microscopic analytical techniques are in general

insensitive to light elements and the measured C, O and N contents might be overestimated due to ambient contamination containing carbonate groups.

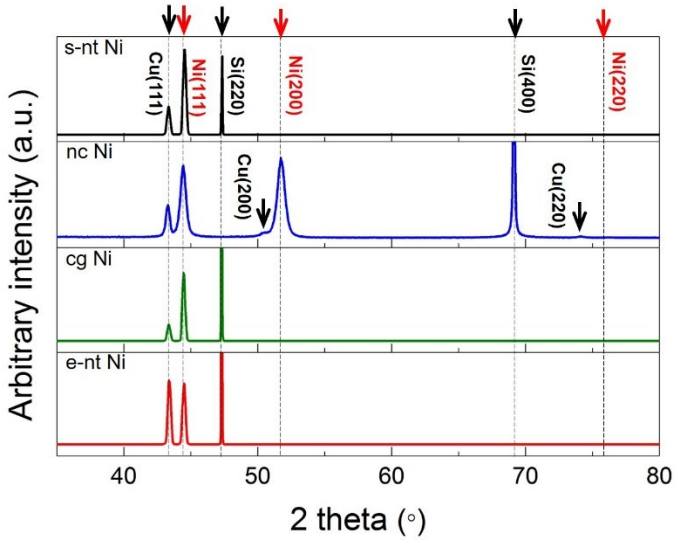

Figure S2. XRD profiles of as-fabricated four Ni specimens including s-nt Ni (sputtered nt Ni on Cu(111)@Si(110)), nc Ni (additive-assisted electrodeposited, abbreviated to AAEP hereafter, Ni on polycrystalline Cu@SiO_2), cg Ni (electrodeposited Ni on Cu(111)@Si(110)) and e-nt Ni (AAEP Ni on Cu(111)@Si(110)). Note: s-nt Ni, nc Ni, cg Ni and e-nt Ni stand for sputtered nanotwinned Ni, nanocrystalline Ni, coarse-grained Ni and electrodeposited nanotwinned Ni, respectively. SiO_2 substrate for nc Ni growth is 100 nm SiO_2 onto 500 μm thick Si(100).

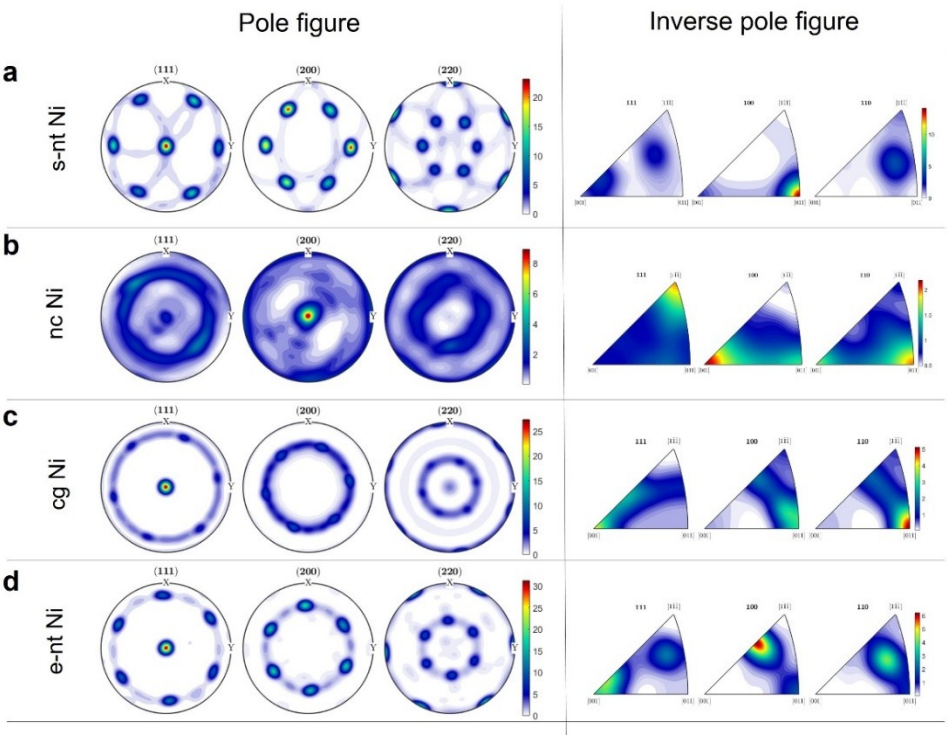

Figure S3. {111}, {200} and {220} Pole figures and corresponding inverse pole figures of (a) s-nt Ni, (b) nc Ni, (c) cg Ni and (d) e-nt Ni.

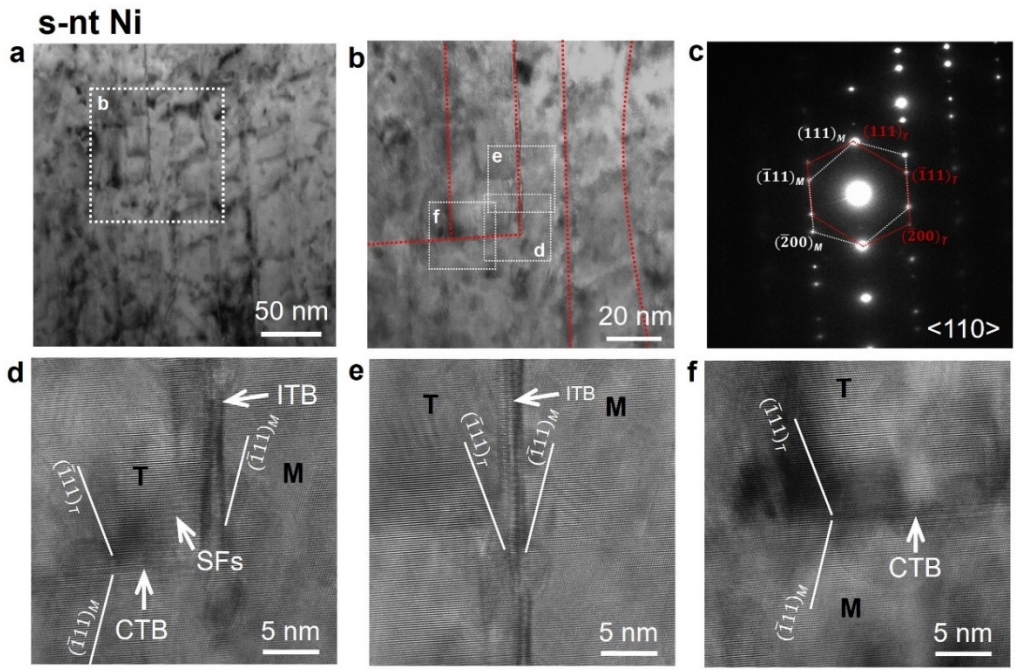

Figure S4. Microstructure of s-nt Ni with giant twins. (a) The cross-section TEM image shows columnar grains with columnar grain size of ~ 30 ± 15 nm. (b) The magnified TEM image suggests that the columnar grain boundaries are comprised of long ITBs and low angle grain boundaries. (c) SAED pattern shows typical twin diffraction pattern in (111)-textured s-nt Ni. (d) HRTEM image shows that s-nt Ni possess large twin structure separated from matrices by long CTBs and ITBs. The twin spacing between CTBs is estimated 182 ± 118 nm. The vertical ITBs intersect with horizontal CTBs, in good agreement with the XFIB image in Figure 1a. (e) HRTEM image highlights one long vertical ITB which has dissociative character. (f) HRTEM shows a typical CTB decorated with SFs.

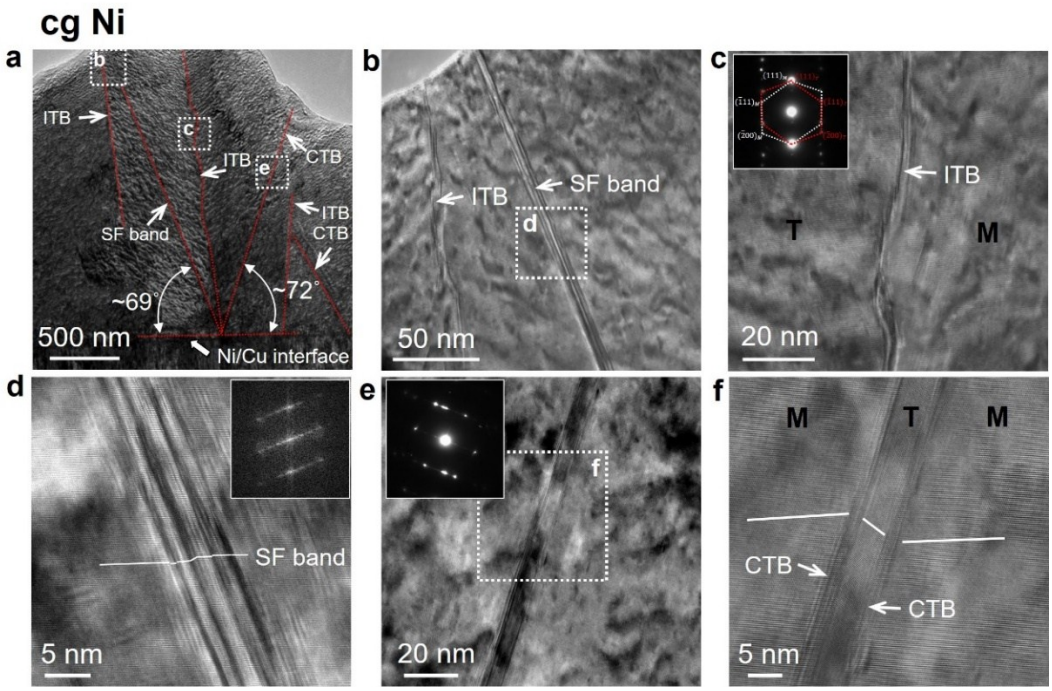

Figure S5. Microstructure of cg Ni with inclined CTBs in large grains. **(a)** The low magnification cross-section TEM micrograph shows ITBs due to grain impingement and SF activities and inclined CTBs on inclined {111} planes with respect to out-of-plane (111). **(b)** The magnified TEM micrograph highlights one curved ITB and SF activities on inclined {111} planes. **(c)** Magnified TEM image and SAD show curved ITB structure. **(d)** On the inclined glide plane $(\bar{1}11)$, the SF activities are identified as SF bands, further verified by the continuous diffraction spots in FFT pattern. **(e)** TEM image shows a typical inclined twin structure with narrow spacing. The SAD suggests typical twin relation and the matrix and twin have mirror-symmetry with respect to $(\bar{1}11)$ planes. The present fine twin is 5-8 nm-thick within grains with average 454 ± 348 nm grain size. **(f)** HRTEM image reveals that inclined CTBs are decorated with some SF ribbons. Note that cg Ni has been prepared using the same electrochemical parameters except that no additive was added into aqueous solution.

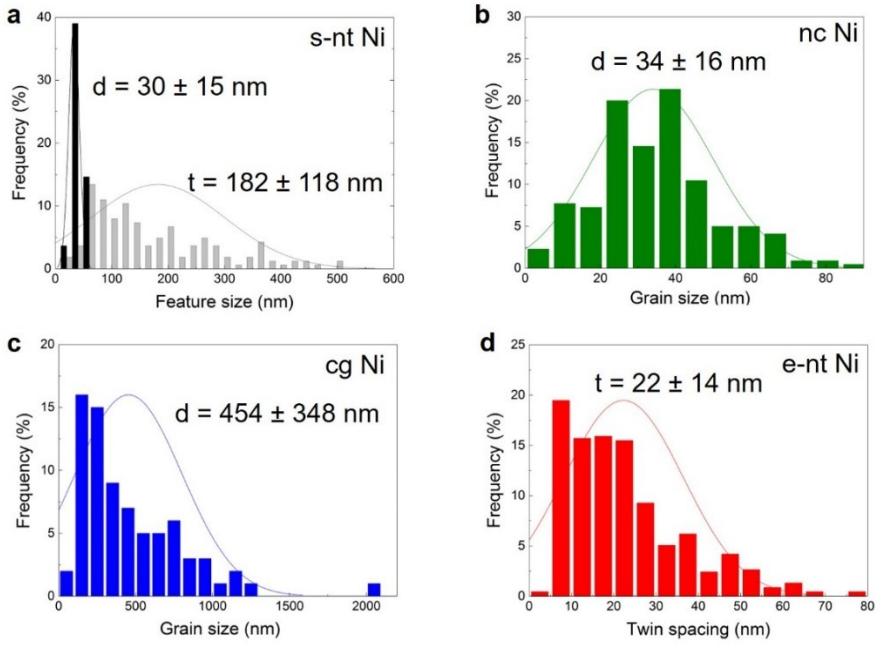

Figure S6. Statistics of structural feature sizes of various Ni specimens: (a) s-nt Ni, (b) nc Ni, (c) cg Ni and (d) e-nt Ni. Note: Columnar/equiaxed grain boundary spacing and twin spacing are selected to represent feature size for different sample. Size distribution has been calculated using Gaussian distribution under the central limit theorem.

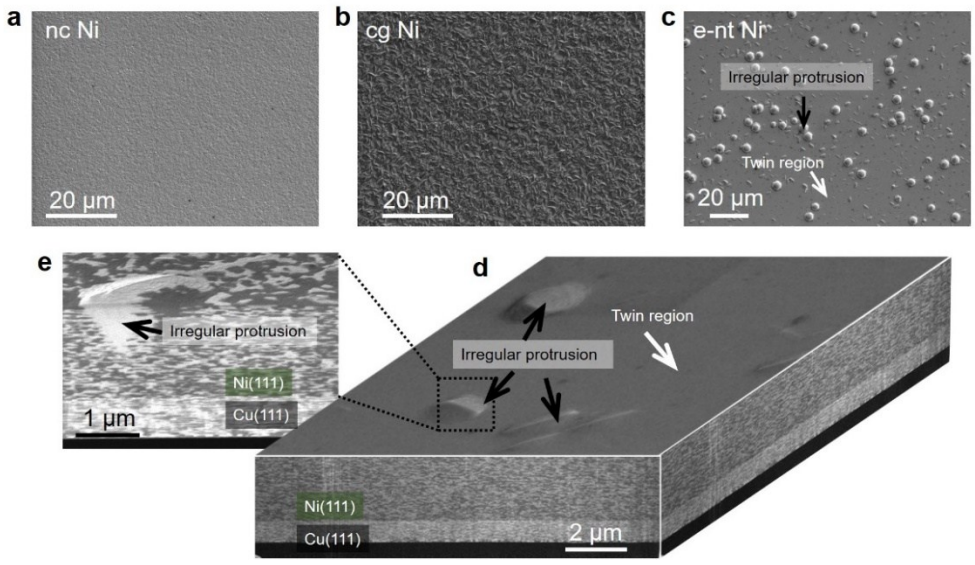

Figure S7. SEM images: surface morphology of (a) nc Ni, (b) cg Ni and (c) e-nt Ni. Besides flat areas underneath which nanoscale twins grow, some irregular protrusions can be seen as isolated islands amid twin structures. (e, d) FIB images showing typical twin structure and some surface protrusions.

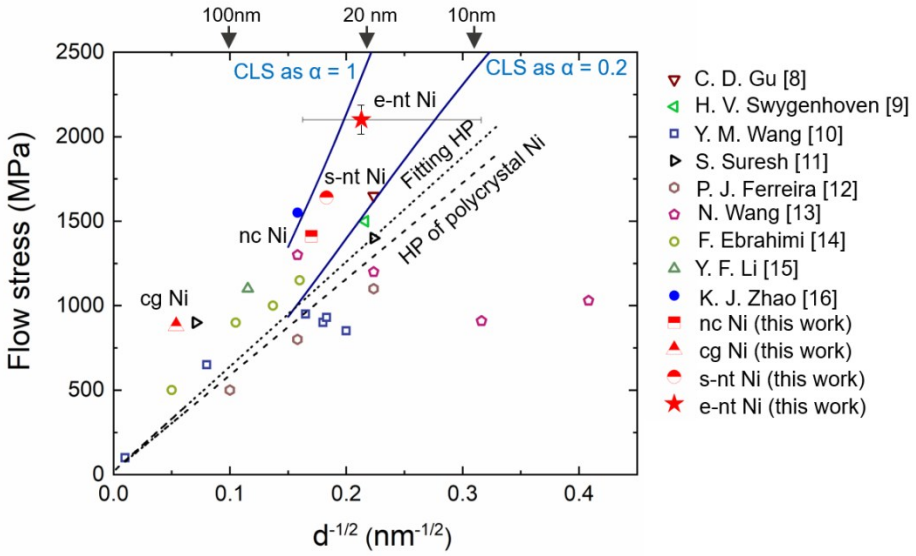

Figure S8. The Hall-Petch plot for four as-deposited Ni specimens. The selected flow stresses from tensile and compressive experiments on cg, ufg, nc and nt pure Ni specimens mainly processed by electrodeposition and plasma vapor deposition are collected from literature [7-15]. It is evident that Hall-Petch strengthening alone cannot explain the high strength of e-nt Ni.

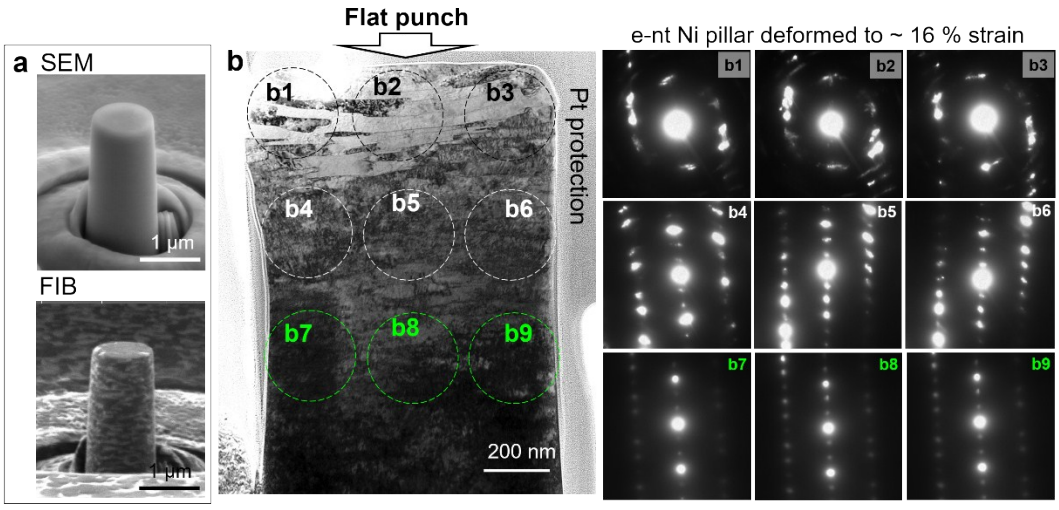

Figure S9. (a) SEM and XFIB images of one e-nt Ni micropillar before deformation. The Cu with lower stiffness would cause preferential buckling of Cu if incorporated into micropillars. Micropillars fabricated through this study solely contain Ni. The material of pillar base is mostly Ni. (b) Post-mortem XTEM micrograph of the e-nt Ni micropillar deformed up to ~16 % strain and SAD patterns selected from different sites showing preferential straining-induced lattice rotation close to the upper portion.

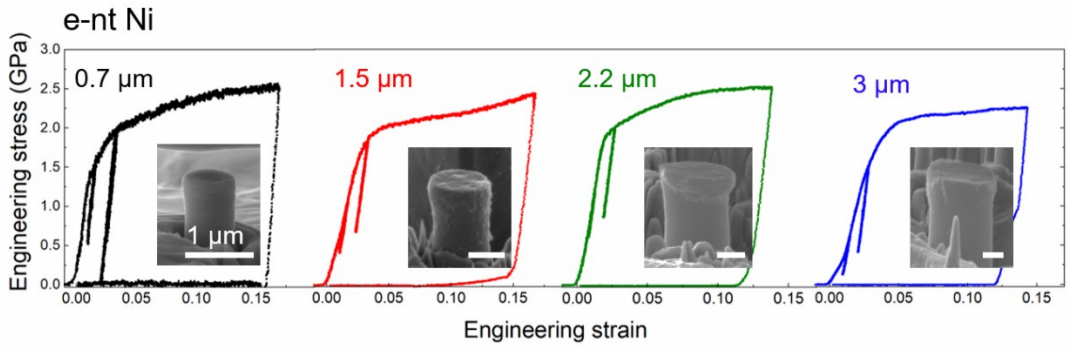

Figure S10. Engineering stress-strain curves from *in situ* compression experiments on e-nt Ni samples with a diameter at middle height of micropillar of 0.7, 1.5, 2.2 and 3 μm to inspect extrinsic size effect.

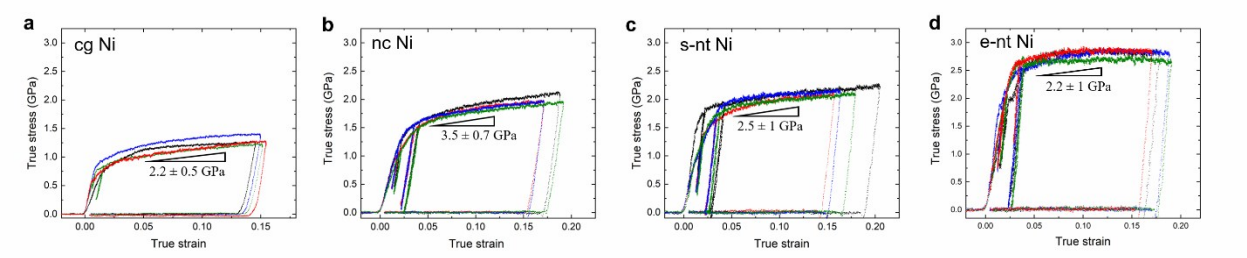

Figure S11. Spontaneous true stress *vs.* true strain curves of cg Ni, (b) nc Ni, (c) s-nt Ni and (d) e-nt Ni, deduced from analyses on real-time deformation by measuring spontaneous punch-pillar contact diameter as a function of displacement (the calculation details were described in text portion of the supplementary information). The calculation reveals that the hardening rate, taken as the slope of the flow stress increment over strain increment (5 – 12 %) for cg Ni, nc Ni, s-nt Ni and e-nt Ni are ~ 2.2, 3.5, 2.5 and 2.2 GPa, respectively.

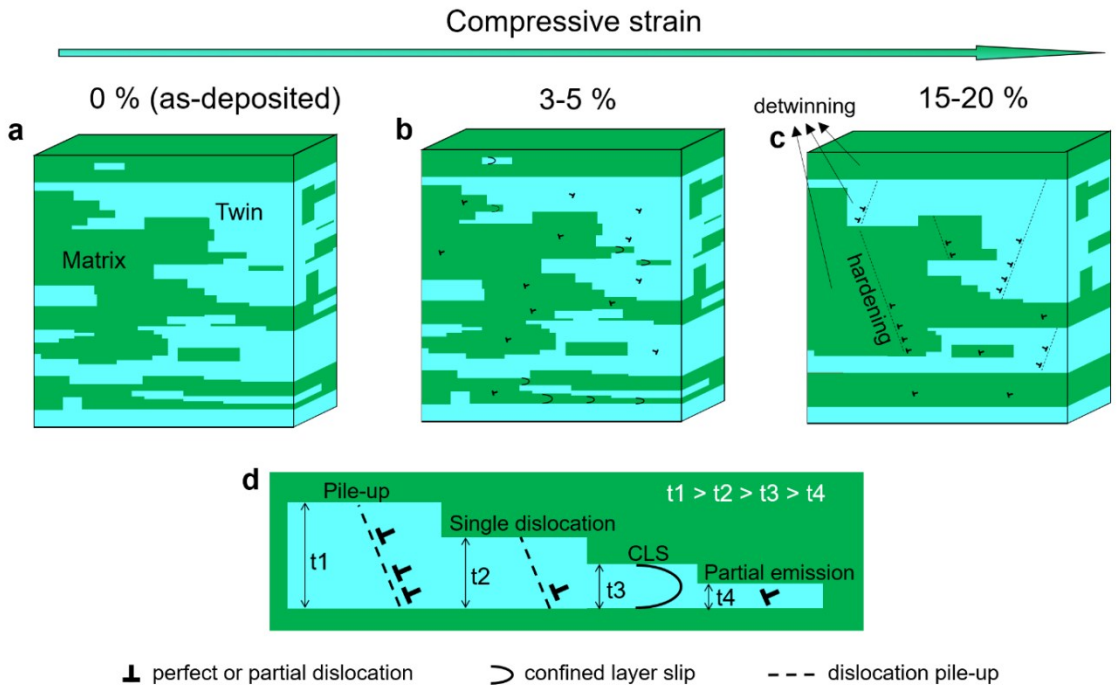

Figure S12. Schematics illustrate the strengthening and deformation mechanisms by manifesting dislocation activities at different strains under compression: (a) 0 % strain where e-nt Ni shows typical GB-free, hierarchical twin structure composed of CTB and ITB segments and twin spacing spreads from few nanometers to about 100 nm; (b) 3-5 % strain where e-nt Ni plastically yields. The regimes with different length scales would nucleate dislocations at different critical stresses, suggestive of there being microplasticity even before global yielding event. Under a uniaxial compression, σ_{yy}, normal to horizontal CTBs, the dislocation activities happen on inclined {111} planes in both matrices and twins in light of both slip planes and slip directions being inclined to CTBs, whereas dislocation cores might spread along CTBs and migrant in confined layer slip (CLS) model as twin spacing is few nanometers or larger; (c) 15-20 % strain where deformation induces plane bending results in a resolved shear component, τ_{yx}, at horizontal (111) planes, which causes ITB migration. The cumulative ITB migration would lead to detwinning and coarsen twin structure and the regimes with larger twin spacing at larger strain levels are sites for dislocation pile-up that results in a more homogeneous deformation process and thus improve deformability. (d) Schematic showing that different deformation mechanism at changing twin spacing in the e-nt Ni with hierarchical twin structures.

Table S1. Experimental and texture conditions of the as-fabricated four Ni specimens.

Specimen name	Fabrication technique	Template	Additive-assisted (Y/N)	Texture
s-nt Ni	Sputtering	Cu(111)		Ni(111)
nc Ni	Hybrid	Poly-Cu	Y	Ni(200)&(111)
cg Ni	Hybrid	Cu(111)	N	Ni(111)
e-nt Ni	Hybrid	Cu(111)	Y	Ni(111)

Note: Poly stands for polycrystalline.

Table S2. Structural information and mechanical responses of the as-fabricated four Ni specimens.

Specimen name	Grain size, d (nm)	Twin spacing, t (nm)	Twin plane orientation	Yield strength, σ_Y (GPa)	Flow stress (5% strain), σ (GPa)	Hardening rate (5-12 %) (GPa)
s-nt Ni	30 ± 15	182 ± 118	Horizontal	1.39 ± 0.08	1.64 ± 0.07	2.5 ± 1
nc Ni	34 ± 16		Random	1.22 ± 0.07	1.41 ±0.04	2.2 ± 0.5
cg Ni	454 ± 348	33 ± 26	Inclined by ~70˚	0.6 ± 0.1	0.88 ± 0.1	3.5 ± 0.7
e-nt Ni		22 ± 14	Horizontal	1.91 ± 0.07	2.1 ± 0.07	2.2 ± 1

Table S3. Potentiodynamic corrosion results for various Ni specimens in 3.5 wt.% of NaCl solution.

Specimen name	E_{corr} (mV)	i_{corr} (A/cm²)	B_a (V/decade)	B_c (V/decade)	R_p (kΩ)	V_{corr} (milli-inch per yea)
s-nt Ni	-210	9.13×10^{-8}	0.092	0.09	216	36×10^{-3}
nc Ni	-192	1.24×10^{-6}	0.512	0.081	24	502×10^{-3}
Bulk-cg Ni	-200	1.59×10^{-7}	0.494	0.087	202	64×10^{-3}
e-nt Ni	-166	6.91×10^{-8}	0.413	0.103	516	28×10^{-3}

Note: E_{corr}, i_{corr}, B_a, B_c, R_p and V_{corr} are corrosive potential, corrosive current density, anodic and cathodic Tafel slopes, polarization resistance and corrosion rate, respectively.

References

1. Stern, M.; Geary, A. L. *J Electrochem Soc* **1957,** 104, (1), 56-63.
2. Sneddon, I. N. *International Journal of Engineering Science* **1965,** 3, (1).
3. Han, S. M.; Phillips, M. A.; Nix, W. D. *Acta Mater* **2009,** 57, (15), 4473-4490.
4. Thomas, S. L.; King, A. H.; Srolovitz, D. J. *Acta Mater* **2016,** 113, 301-310.
5. Liu, L.; Wang, J.; Gong, S. K.; Mao, S. X. *Phys Rev Lett* **2011,** 106, (17).
6. Wang, J.; Misra, A.; Hirth, J. P. *Phys Rev B* **2011,** 83, (6).
7. Gu, C. D.; Lian, J. S.; Jiang, Q.; Zheng, W. T. *J Phys D Appl Phys* **2007,** 40, (23), 7440-7446.
8. Dalla Torre, F.; Van Swygenhoven, H.; Victoria, M. *Acta Mater* **2002,** 50, (15), 3957-3970.
9. Wang, Y. M.; Ott, R. T.; van Buuren, T.; Willey, T. M.; Biener, M. M.; Hamza, A. V. *Phys Rev B* **2012,** 85, (1).
10. Schwaiger, R.; Moser, B.; Dao, M.; Chollacoop, N.; Suresh, S. *Acta Mater* **2003,** 51, (17), 5159-5172.

11. Carlton, C. E.; Ferreira, P. J. *Acta Mater* **2007,** 55, (11), 3749-3756.
12. Wang, N.; Wang, Z. R.; Aust, K. T.; Erb, U. *Mat Sci Eng a-Struct* **1997,** 237, (2), 150-158.
13. Ebrahimi, F.; Bourne, G. R.; Kelly, M. S.; Matthews, T. E. *Nanostruct Mater* **1999,** 11, (3), 343-350.
14. Zhu, R. T.; Li, Y. F. *Rare Metal Mat Eng* **2016,** 45, (7), 1654-1658.
15. Zhang, Y. F.; Wang, J.; Shan, H. Q.; Zhao, K. J. *Scripta Mater* **2015,** 108, 35-39.